Dislocations and their stress field in natural peridotites from the palaeosubduction interface of the Oman-UAE ophiolite

M. K. Sep
Utrecht University
09−02−2020

Abstract

Major seismic events induce period of transient creep, during which the effective viscosity of the rocks evolves with time, before steady-state creep is reached. Recent experimental work on olivine deformation resulted in a new rheological model for transient and steady-state creep based on back stresses between dislocations. However, observational research on structures in natural rocks that support this new model have not yet been conducted. Here, I analyse natural peridotites from the Oman-UAE ophiolite, where microstructural evidence for the processes involved in transient creep is potentially preserved, to compare their microstructures to those formed by experimental olivine deformation. This research uses oxidation decoration and high-angular resolution electron backscatter diffraction to characterise the microstructure and to map 'free' dislocation densities and stress heterogeneities. The results reveal banded structures of high dislocation densities, often bounded by subgrain boundaries and colocated with high stress heterogeneities of hundreds of megapascals over length scales of only a few micrometres. These results combined with the characteristic probability distribution of the stresses indicate that the stress heterogeneities originate from long-range dislocation interactions and that these interactions contribute to the organisation of the substructure. These results are similar to those from the experimental work on transient creep in olivine and support the applicability of the new rheological model to large-scale modelling of plate-boundary fault zones.

1. Introduction

Major seismic events induce a geologically short stage of deformation by transferring stress from the brittle upper crust to the viscoelastic lower crust and upper mantle. This postseismic stage of deformation is often referred to as transient creep during which the strength of the rocks changes until steady-state creep is reached. During transient creep, strain hardening causes the material properties to change significantly, on both small and large scales. Understanding transient creep is therefore important for modelling large-scale geodynamics, where it is one of the processes that influences the strength of the Earth's lithosphere. Strain hardening occurs during both low-temperature plasticity and power-law creep at high temperatures, raising the possibility of a common underlying cause.

Recent experiments on olivine (e.g., Wallis et al., 2017, 2019b, in prep.; Hansen et al., 2019) resulted in a new rheological model based on back stresses between dislocations for transient and steady-state creep, as illustrated in Figure 1 (Hansen et al., in prep.). During transient creep, dislocation glide (lower dashpot) dominates and generates back stresses between dislocations (upper spring). These back stresses cause strain hardening, as it would be increasingly difficult to compress the spring in Figure 1. However, as the back stress builds up, dislocations climb (upper dashpot) will become increasingly relevant. Dislocation climb will eventually catch up with dislocation glide, preventing further accumulation of back stress. This catching up of dislocation climb to dislocation glide is the gradual change from transient creep to steady-state creep. In this model, dislocation climb can be interchanged with dynamic recovery by cross-slip and annihilation of screw dislocations when temperatures are too low for dislocation climb to be relevant, as discussed in Wallis et al. (2019b).

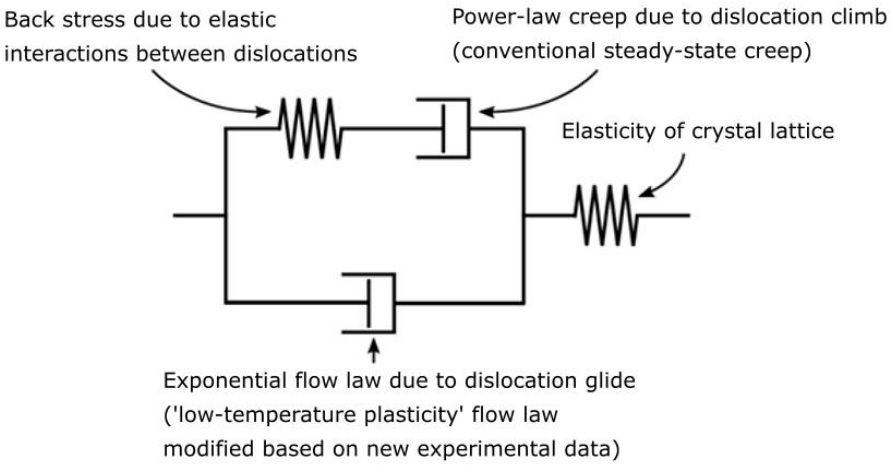

Figure 1: *Illustration of the model for transient and steady-state creep as in Hansen et al. (in prep.) for olivine at low and high temperatures.*

Studies on large-scale, postseismic deformation (e.g., Pollitz 2003; Han et al., 2014; Huang et al., 2014; Sun et al., 2014; Qiu et al., 2018) provide observations of transient creep. The recent study of Qiu et al. (2018), for example, demonstrates that steady-state creep is preceded by approximately two years of transient creep, initiated by earthquakes along the Sumatran subduction zone. In these studies, transient creep is often interpreted as intergranular interactions, following the research on water ice (Duval et al., 1983; Ashby & Duval, 1985; Karato, 1998). Intragranular interactions, such as strain hardening due to the build up of back stress, are however often not addressed (Wallis et al., in prep.). Furthermore, recent models of earthquake triggering (e.g., Field et al., 2015) include long-term, time-dependent stress and strength changes, but are missing short-term, time-dependent stress transfer (Freed, 2005). Understanding transient creep gives the opportunity to improve time-dependent models for earthquake triggering.

However, the microscale processes that generate transient creep remain poorly constrained. Hansen et al. (2019) performed deformation experiments on single crystals and aggregates of olivine at low temperature to investigate the microscale processes related to strain hardening. The experimental research demonstrates that transient creep also occurs in single crystals, highlighting the importance of intragranular processes (Durham et al., 1979; Hanson & Spetzler, 1994; Cooper et al., 2016). The data of the experimental researches provided a basis for the new model for transient and steady-state creep, as explained in Figure 1 (Hansen et al., in prep.). The Bauschinger effect in the mechanical data indicates that strain hardening is caused by long-range interactions between dislocations due to accumulation of back stresses between them (Hansen et al., 2019). Wallis et al. (2019b) analysed the microstructures of the samples of Hansen et al. (2019) and elaborated on the microphysical basis of the flow law. Their research used scanning transmission electron microscopy (STEM), conventional electron backscatter diffraction (EBSD), and high-angular resolution electron backscatter diffraction (HR-EBSD) to investigate the microstructures. The research reveals stress heterogeneities on the order of 1 GPa on a length scale of only a couple micrometres, indicating that these heterogeneities result from long-range interactions between dislocations. Therefore the back stresses are interpreted to be dominant in generating strain hardening at low temperature. This research also provides new microstructural indicators of the processes associated with strain hardening. Further research (Wallis et al., in prep.) demonstrates that similar processes occur at higher temperatures, supporting their relevance to models of transient creep. Analyses of the probability distributions of the residual shear stresses provide a strong indication that the local stress fields are generated by the interactions of dislocations (Wilkinson et al., 2014; Wallis et al., in prep.). The logical next step is to compare these experimental results with natural rocks to assess the evidence for similar microscale processes.

This research analyses samples of deformed peridotites by Ambrose et al. (2018), which originate from the Oman-UAE ophiolite (Figure 2), with the aim to compare their microstructures to those from the experimental samples to test the relevance of the model for transient creep. I test the hypothesis that these deformed peridotites and the experimental samples contain similarities in their microstructures which are caused by strain hardening due to the build up of back stresses. The ophiolite is a geological setting where transient creep likely occurred, as the base of the ophiolite is an exhumed palaeosubduction interface (Agard et al., 2016). Since the ophiolite formed during subduction, it matches the low temperature conditions at which microstructural evidence for transient creep by dislocation-mediated processes is likely well preserved. The samples originate from varying distances from the metamorphic sole as presented in the cross-section in Figure 2B. The peak metamorphic conditions of the metamorphic sole are 770−990°C and 1.1−1.3 GPa and the calculated differential stress using subgrain-size piezometry is 25−35 MPa (Ambrose et al., 2018). The current research uses existing conventional EBSD data by Ambrose et al. (2018) and performs oxidation decoration and HR-EBSD analyses on some of the samples to characterise the microstructures of the deformed peridotites and to reveal intragranular stress heterogeneities.

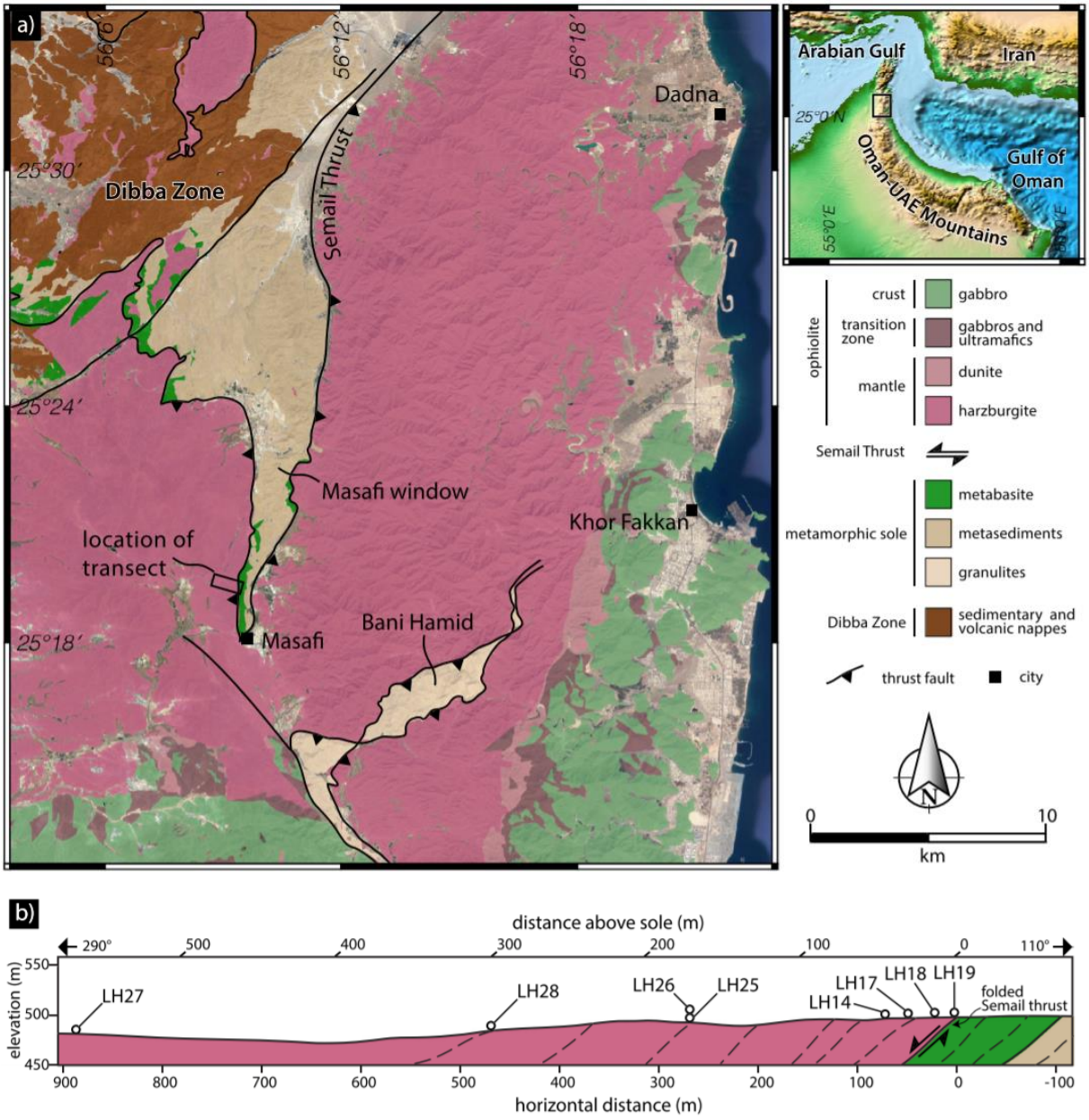

Figure 2: *Location of the sampled area by Ambrose et al. (2018). a) Geological map of the northern UAE displaying the location of the transect. b) Cross section of the sampled area, indicating both the horizontal distance from the metamorphic sole (i.e., the folded Semail thrust) and the distance above the sole which is calculated from the measured foliations. This research uses the horizontal distance to minimize calculation errors. Figures by Ambrose et al. (2018).*

2. Methods

This research uses the eight samples of Ambrose et al. (2018), which originate from varying distances from the metamorphic sole of the ophiolite. The horizontal distance from the sole ranges from 1 m to 888 m (Figure 2B), with a corresponding structural thickness of up to ~490 m. I use conventional electron backscatter diffraction (EBSD) data to analyse the crystallographic preferred orientations (CPOs), the misorientation inverse pole figures (MIPFs) and the misorientation pole figures (MPFs) in detail. Ambrose et al. (2018) collected these EBSD data using an FEI Quanta 650 scanning electron microscope with a field emission gun and an Oxford Instruments Aztec acquisition system and NordlysNano EBSD camera. They used a 30 kV acceleration voltage in low-vacuum mode with a step size of 5 µm (15 µm for LH19).

Dislocations in samples LH18, LH17 and LH28, with distances from the metamorphic sole of 22 m, 51 m and 469 m respectively, were decorated by the oxidation method (Kohlstedt et al., 1976). Pieces were cut from the samples originally polished by Ambrose et al. (2018) and heated in a furnace at 900°C for 45 minutes to oxidise the surface of the samples and dislocation cores. Hand polishing with 30 nm colloidal silica for approximately ten minutes removed the oxidised top layer but left the decorated dislocations visible. A 7 nm Pt/Pd coat was applied to the samples. The samples were imaged using backscattered electrons in an FEI Helios focussed ion beam-scanning electron microscope at Utrecht University, following Karato (1987) on imaging decorated dislocations.

All 'free' dislocations (i.e., dislocations not aligned in subgrain boundaries) in the decorated samples are counted per surface area to determine the dislocation density. I use ten different grains in the three samples to average their densities. Differential stresses are calculated from the dislocation density using

$$\rho = \beta\sigma^m , \quad (1)$$

where ρ is the dislocation density, σ is the differential stress and constants m and β are 1.41 and 1.1×10^9, respectively (Karato & Jung, 2003). These dislocation densities and corresponding differential stresses are calculated on a grain scale and on a substructure scale, where the latter focusses on differences between high and low dislocation-density regions in the grains.

The non-oxidised part of sample LH17 was analysed in more detail using HR-EBSD, to obtain precise measurements on the misorientations. Sample LH17 was selected for HR-EBSD analysis as it has the highest proportion of unserpentinised olivine, is typical of samples that lie on the trends of grain size and minor-phase abundance identified by Ambrose et al. (2018), and originates from close (51 m) to the metamorphic sole. The sample was repolished by hand using 30 nm colloidal silica for 10 minutes and coated with 0.5 nm of Pt/Pd. New EBSD maps for HR-EBSD processing were acquired using Oxford Instruments AZtec 3.3 acquisition software and a NordlysNano EBSD detector on a Phillips XL-30 scanning electron microscope at Utrecht University. Diffraction patterns were acquired using an acceleration voltage of 30 kV, a working distance of 15 mm, and no binning of the 1344 x 1024 pixels in the patterns. The map and step sizes differ per HR-EBSD map, of which the details are in the description of the figures in the results section.

HR-EBSD is a postprocessing technique that uses high-quality conventional EBSD data (i.e., highest quality surface preparation, accurate and precise knowledge on the pattern centre while under the electron microscope and minimal binning and gain) to measure lattice rotations and elastic strains and to calculate the geometrically necessary dislocation (GND) densities and residual stresses (Wilkinson et al., 2006; Britton & Wilkinson, 2011, 2012; Wallis et al., 2019a). HR-EBSD uses the stored diffraction

patterns to measure the lattice rotations and elastic strains by using one reference point in each grain in the mapped area. In the diffraction pattern of this reference point, multiple regions of interest (ROIs) are collected. These ROIs in the reference point are compared to the ROIs in each other point in the grain via cross correlation, resulting in displacements between the reference pattern and the pattern in each point in the grain. These displacements are broken down into components of lattice rotations and elastic strains (Wilkinson et al., 2006; Britton & Wilkinson, 2011, 2012; Wallis et al., 2019a). The lattice rotations are used to estimate the GND densities, since GNDs result in lattice curvature (Wallis et al., 2016). These GND densities are grouped in the six possible dislocation types in olivine, because each dislocation type causes a different curvature. The elastic strains are used to calculate residual stresses, using Hooke's law and the elastic stiffness tensor (Wallis et al., 2017, 2019a). The elastic strains and residual stresses are relative to the unknown strain and stress state of the reference point and therefore the mean of each stress component is normalized to zero (Jiang et al., 2013; Mikami et al., 2015; Wallis et al., 2017). This means that the residual stresses only report the stress heterogeneity in each grain.

I used the normalised shear stresses, σ_{12}, obtained by HR-EBSD, to calculate the restricted second moment, ν_2. The restricted second moment is calculated with

$$\nu_2(\sigma) = \int_{-\sigma}^{+\sigma} P(\sigma)\sigma \mathrm{d}\sigma \quad , \tag{2}$$

where the probability $P(\sigma)$ is integrated over restricted stress ranges (Groma & Bakó, 1998; Wilkinson et al., 2014). At high stresses, the restricted second moment should plot as straight lines against the natural logarithm of the shear stress, indicating that

$$P(\sigma) \propto \sigma^{-3}. \tag{3}$$

This is the expected result for stress fields generated by dislocations (Groma & Bakó, 1998; Wilkinson et al., 2014; Wallis et al., in prep.).

3. Results

3.1 Conventional EBSD

Figure 3 presents the pole figures of the crystallographic preferred orientations (CPOs) of all eight samples by Ambrose et al. (2018), obtained by conventional EBSD. The comparison between the observed CPO pole figures and those of Bernard et al. (2019) results in an overall dominant B-type CPO, related to a dominant (010)[001] dislocation type. The CPO type is most clear in the samples closest to the metamorphic sole. Samples LH25 and LH26, at 266 m from the sole, are closer related to an E-type CPO with a dominant (001)[100] dislocation type.

Figure 3 also presents the misorientation inverse pole figures (MIPFs), plotting the axes of misorientations with angles between 4 and 10 degrees, representing subgrain boundaries. Misorientations larger than 10 degrees are more likely to represent grain boundaries and misorientations smaller than 4 degrees are more influenced by noise. The main peaks in the figures are most commonly centred on the [010] axis. [010] rotation axes can be generated by tilt walls composed of the (001)[100] and/or (100)[001] edge dislocation types, where the crystal lattice rotates around the [010] axis (e.g., Wallis et al., 2017, Figures 2C & 2D). In most samples, the peaks at [010] are part of a band of elevated densities between the [010] and [001] axes. This band is often interpreted as indicating the operation of “pencil glide” on the (0*kl*)[100] slip systems (De Kloe et al., 2002). Further from the metamorphic sole, peaks around [101] and [410] are observed as well. Sample LH27, at a distance of 888 m from the metamorphic sole, is the only sample where the [010] peak and the “pencil glide” are not observed.

The misorientation pole figures (MPFs) in Figure 3 reveal peaks between the centre and the top of the pole figure. For materials deformed in simple shear, the misorientation axes should plot in the centre for tilt walls and at the top for twist walls. Therefore, these results suggest a combination of screw and edge dislocation types in subgrain boundaries. The peaks in most of the MPFs plot on the north-south axis. This suggests that the angle between the assumed foliation by Ambrose et al. (2017) and the actual foliation of the rock is negligible. If there is such an angle, than the peaks would slightly shift towards the west or the east in the pole figures. This shift is however observed in sample LH17 and to a minor extent in samples LH18 and LH19. This shift means that, if corrected by a back rotation, the results of the CPO pole figures might also slightly shift, which would only be significant for the LH17 sample. The CPO pole figures for LH17 can however not be reconstructed back to what it should be, since the MPF for this sample does not result in one peak, but in a band of higher values.

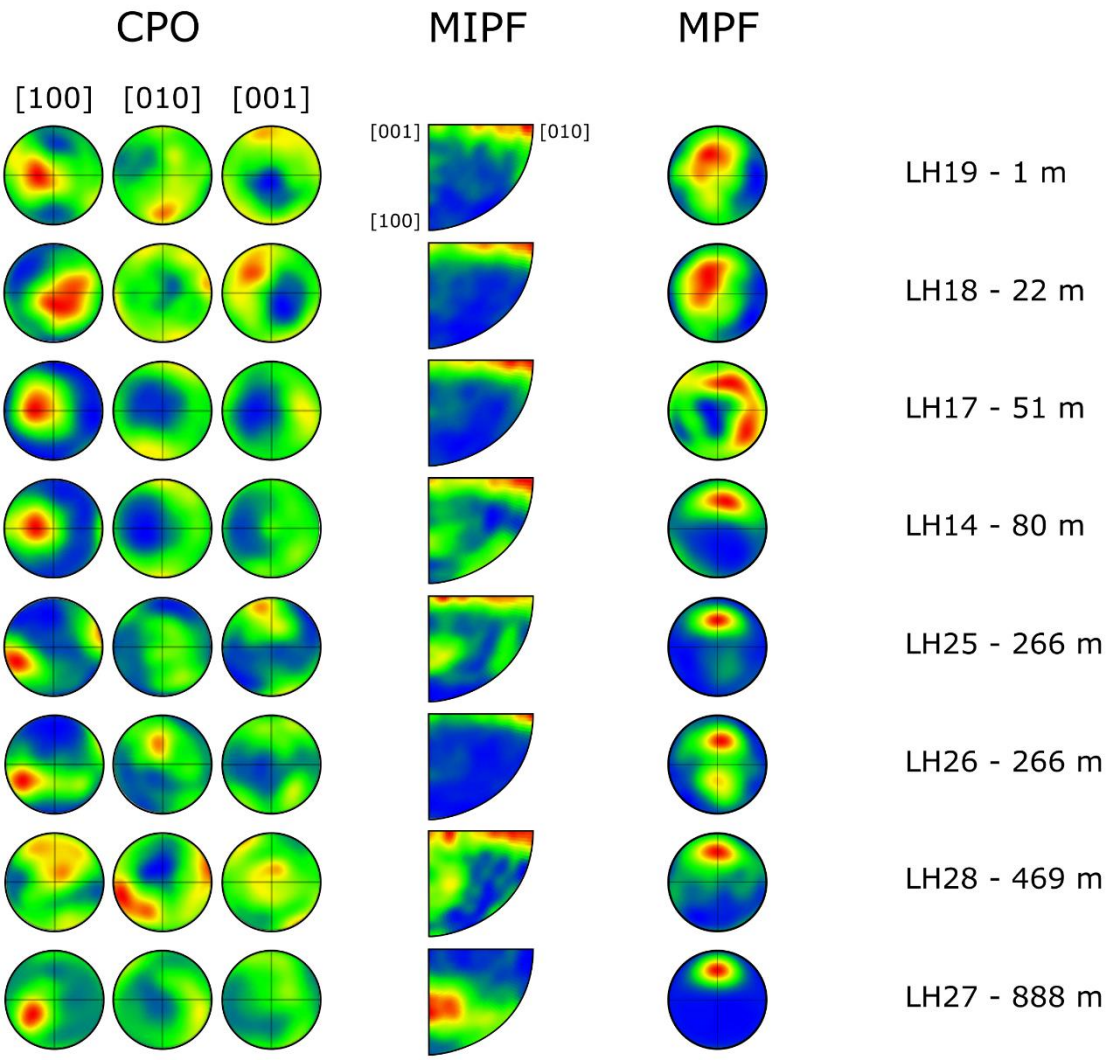

Figure 3: *Results of conventional EBSD analysis listed by distance from the metamorphic sole. The first column presents the crystallographic preferred orientation (CPO) pole figures. The second column presents the misorientation inverse pole figures (MIPFs) of local misorientations of 4 to 10 degrees. The third column presents the misorientation pole figures (MPFs).*

3.2 Oxidation decoration

Figure 4 presents six representative images of the oxidation decorated samples, with two images for each of the three samples. All samples contain grains where the dislocations occur in bands, approximately 3.5 μm wide, with dislocation densities that are higher than average, which are most clear in Figures 4C, 4D and 4E. These bands are often bounded by a subgrain boundary on one side of the band, marking an abrupt change in dislocation density (e.g., Figure 4E, where the topmost band of high density is bounded at its bottom by a line of closely spaced points, interpreted as a subgrain boundary). Other subgrain boundaries outside the banded structures are orientated in the same direction as the banded structures.

Figure 4A is less clear compared to Figures 4C, 4D and 4E, but also contains banded structures and subgrain boundaries, both in a vertical orientation. A more chaotic set of dislocations forms at least two diagonal bands in Figure 4A, which seems to be a different structure than the more ordered vertical structure. I also observe a similar relationship in Figure 4C, where the banded structures in the top right of the figure converge to the chaotic set of dislocations in the bottom left.

Figure 4F also reveals heterogeneity between the left and right parts of the figure. The right part contains aligned dislocations in vertically orientated subgrain boundaries. However, the left part contains curved dislocations of different orientations, which are interacting with each other to form a tangled structure.

Table 1 contains the results of the analysis on the dislocation densities and the differential stresses calculated from these densities using equation (1). The table includes the six grains presented in Figure 4, as well as four other grains which are presented in the appendix. These results demonstrate that the dislocation densities from grain to grain can differ by an order of magnitude, but that the averages are relatively similar. The average dislocation density of the three samples is 1.4×10^{12} m^{-2}, resulting in an average differential stress of 160 MPa. Table 1 also demonstrates the differences in dislocation density and differential stress between the high and low dislocation-density regions (i.e., inside and outside the banded structure), resulting in stress heterogeneities of several hundreds of megapascals over distances of several micrometres.

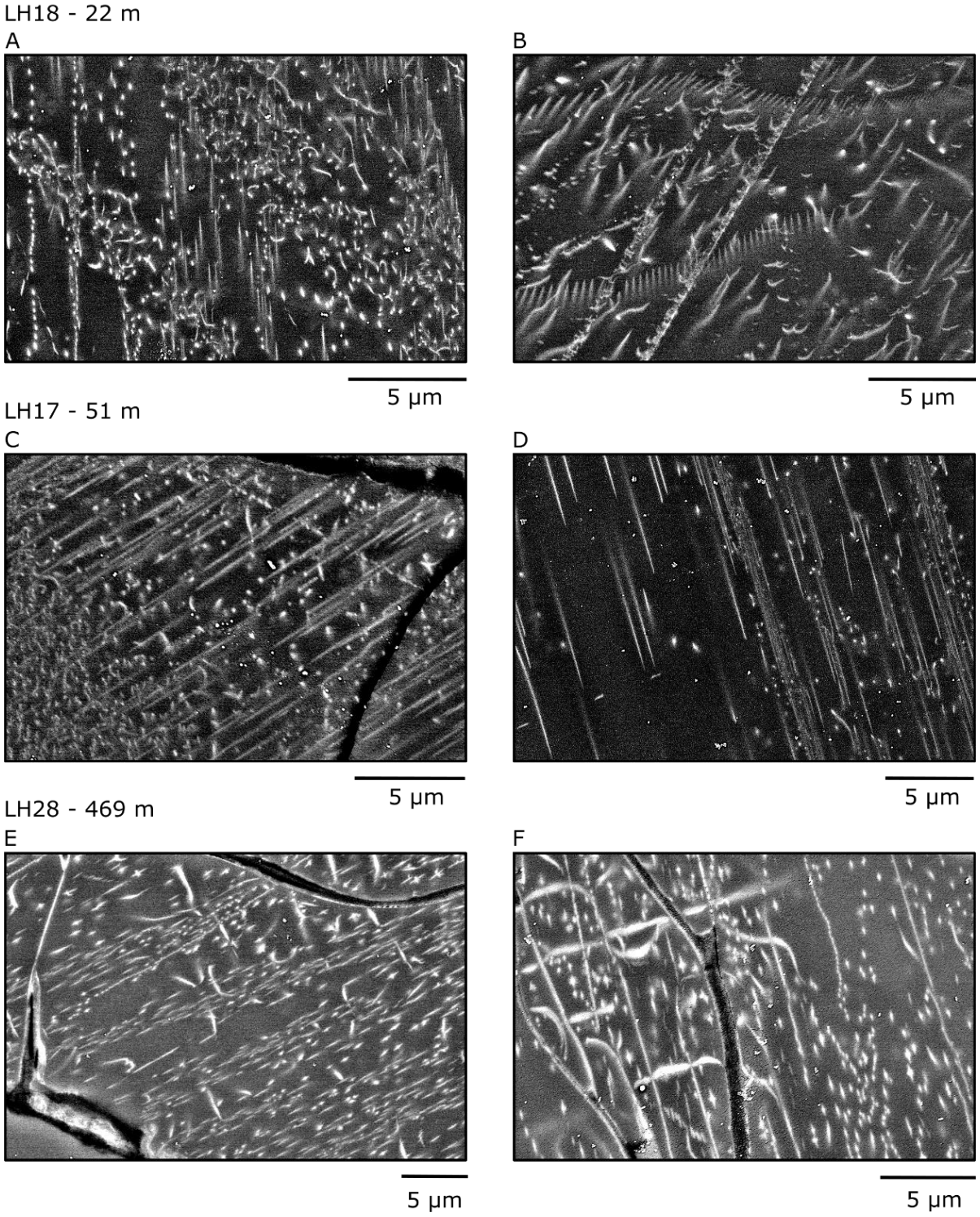

Figure 4: *Results of oxidation decorated samples. Figures A and B have a distance of 22 m from the sole, C and D have a distance of 51 m from the sole and E and F have a distance of 469 from the sole. Overview figures and additional figures are presented in the appendix.*

Table 1:
Results from the dislocation density analysis and the calculated differential stresses. The maps of the decorated dislocations used in the analysis can be found in the appendix.

Grain	Dislocation density (m^{-2})	Low density (m^{-2})	High density (m^{-2})		Differential stress (MPa)	Low stress (MPa)	High stress (MPa)
LH18_001	1.90×10^{12}	3.27×10^{11}	5.15×10^{12}		198.46	56.93	401.65
LH18_004	1.13×10^{12}				137.12		
LH18 average	1.52×10^{12}				168.94		
LH17_001	6.02×10^{11}	2.82×10^{11}	1.05×10^{12}		87.68	51.19	130.33
LH17_015	2.34×10^{12}	1.77×10^{12}	2.95×10^{12}		229.79	188.43	270.70
LH17_023	2.73×10^{12}	1.09×10^{12}	4.13×10^{12}		256.54	133.95	343.40
LH17_027	8.57×10^{11}	1.34×10^{11}	1.87×10^{12}		112.68	30.25	196.23
LH17 average	1.63×10^{12}				178.03		
LH28_004	1.47×10^{12}				164.89		
LH28_008	1.09×10^{12}	6.89×10^{11}	1.65×10^{12}		133.25	96.55	179.64
LH28_013	9.94×10^{11}	4.69×10^{11}	1.36×10^{12}		125.14	73.49	155.95
LH28_018	9.09×10^{11}	5.63×10^{11}	1.17×10^{12}		117.45	83.67	140.07
LH28 average	1.11×10^{12}				135.67		

3.3 HR-EBSD

Figure 5 presents the results of the HR-EBSD analysis of an olivine grain in sample LH17, located 51 m from the metamorphic sole. It presents maps for the GND density of each dislocation type, the lattice rotations and the residual stresses. Sub-vertical bands, perpendicular to the [100] axis of the orientation of the grain, of elevated GND density dominate the structure of the grain. The maps on the top row, representing the dislocation types with a [100] burgers vector, reveal that the sign of the burgers vector changes in the middle of the grain (i.e., red coloured bands change to blue coloured bands). The maps of the lattice rotation in Figure 5 illustrate the result of the changing sign of the burgers vectors in the grain. From left to right the lattice rotates in one direction until it reaches the middle of the grain, where the lattice rotates back again. The bottom three maps of Figure 5 present the residual stresses in the grain, which turn out to be very pixelated because of the large step-size.

The HR-EBSD results presented in Figure 6 originate from the same grain as Figure 5, but zoomed in on a scratch-free area including a subgrain boundary separating the left part with a higher GND density from the right part with a lower GND density. The observation of a subgrain boundary separating a higher from a lower density matches the similar observation in oxidation decoration, on a similar length scale (Figure 4). There are two bands of elevated GND density with opposing signs for the burgers vector on the left side of the subgrain boundary for all dislocation types with a [100] burgers vector. The GND density of the band in between the two opposing bands is relatively low. The GND density maps for the dislocation types with a [001] burgers vector have low GND densities and do not reveal a clear structure, except for the subgrain boundary. The shear stress map (σ_{12}) in Figure 6 reveals an increase in stress from left to right, until the subgrain boundary is reached. To the right of this boundary the stress drops significantly and is more uniform. The local stress heterogeneity observed here is around 500 MPa over distances of a few micrometres.

Figure 7 presents the HR-EBSD maps of a different grain in the same sample as Figures 5 and 6. The GND maps reveal bands of high GND density of approximately 3 microns wide with an orientation perpendicular to the [100] axis. The lattice rotation maps reveal diagonal lines where the lattice rotation suddenly changes, indicating subgrain boundaries. The [100] screw and the (010)[100] edge slip systems reveal opposing burgers vectors on each side of the subgrain boundaries. The maps of [001] screw and (010)[001] edge dislocations also reveal opposing burgers vectors on either side of the subgrain boundaries, but the burgers vectors of these dislocation types are parallel to the subgrain boundaries. The (001)[100] edge and (100)[001] edge dislocations do not reveal opposing burgers vectors and these two dislocation types seem to be more in between of the subgrain boundaries. The map of the shear stress (σ_{12}) in Figure 7 demonstrates that the stress heterogeneity is mainly located near the bands of elevated GND density, reaching a couple hundreds of megapascals over a micrometre length scale perpendicular to the banded structure.

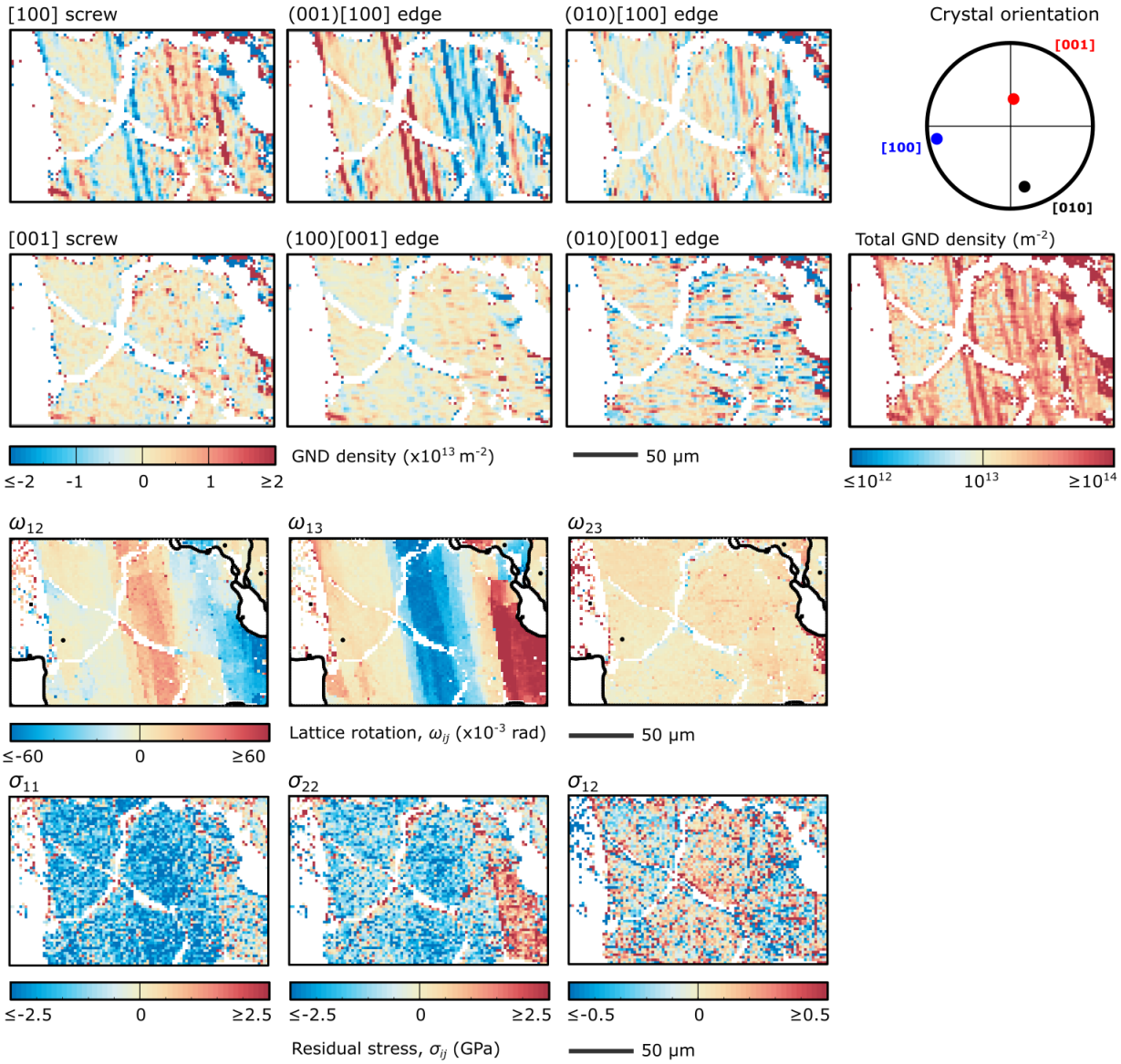

Figure 5: *LH17_HR. HR-EBSD results of a grain in sample LH17, located 51 m from the metamorphic sole. The six maps at the top present the GND densities of the different dislocation types, where the colours indicate opposing signs of the burgers vector. The crystal orientation is presented in the top right and below it the total GND density is presented. The third row of maps presents the lattice rotation, ω_{ij}, in which grain boundaries (i.e., local misorientations greater than 10 degrees) are revealed as black lines. The black dot indicates the reference point for the calculations of the lattice rotations. The bottom row presents the maps of the residual stresses, σ_{ij}, where σ_{12} represents the residual shear stress. The step size is 2 μm and the number of datapoints is 6500 (100×65).*

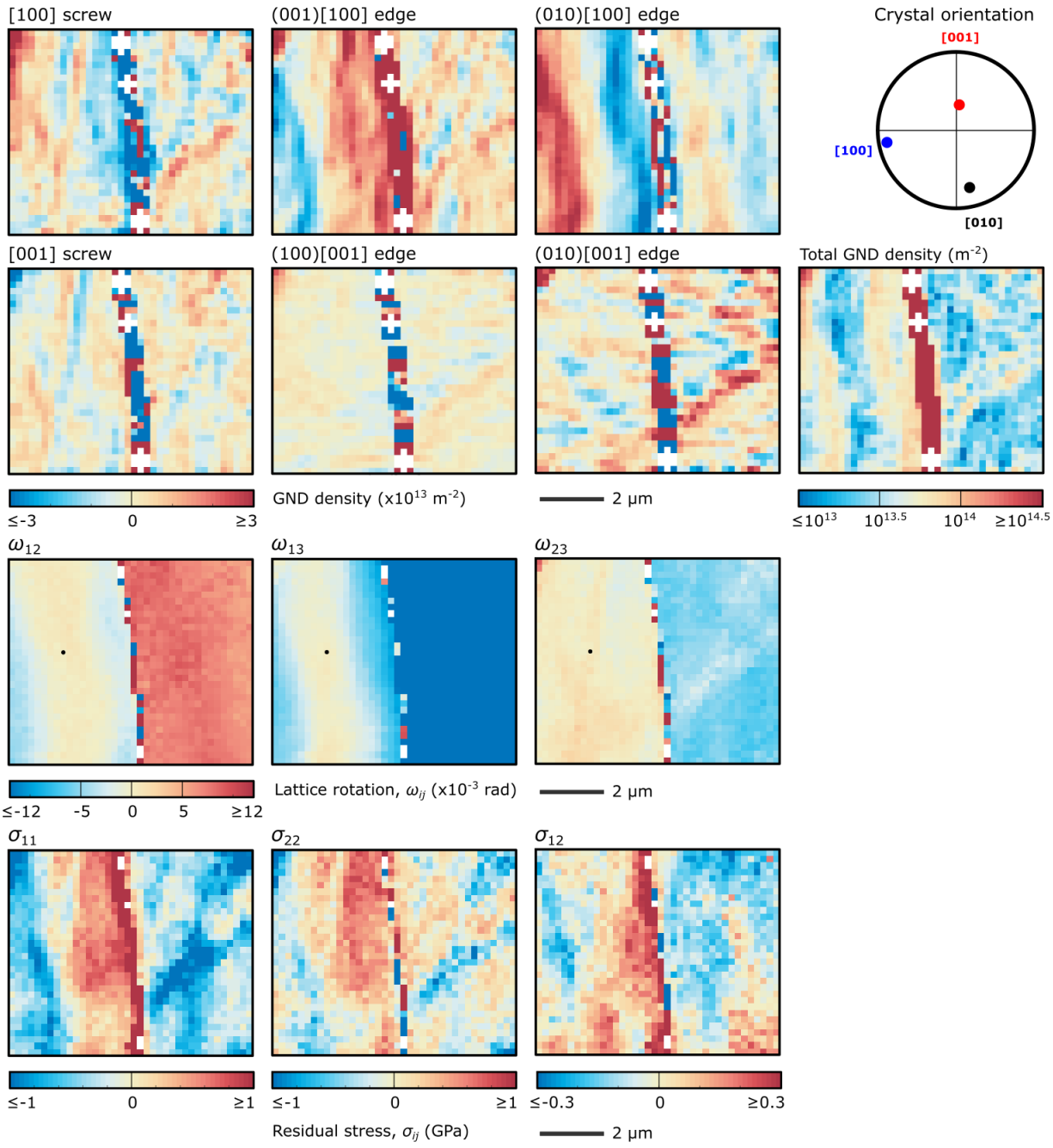

Figure 6: *LH17_HR4_map2. HR-EBSD results of the same grain in sample LH17 as Figure 5, but zoomed in on a scratch free part. The six maps at the top present the GND densities of the different dislocation types, where the colours indicate opposing signs of the burgers vector. The crystal orientation is presented in the top right and below it the total GND density is presented. The third row of maps presents the lattice rotation, ω_{ij}. The black dot indicates the reference point for the calculations of the lattice rotations. The bottom row presents the maps of the residual stresses, σ_{ij}, where σ_{12} represents the residual shear stress. The step size is 0.2 μm and the number of datapoints is 1216 (32×36).*

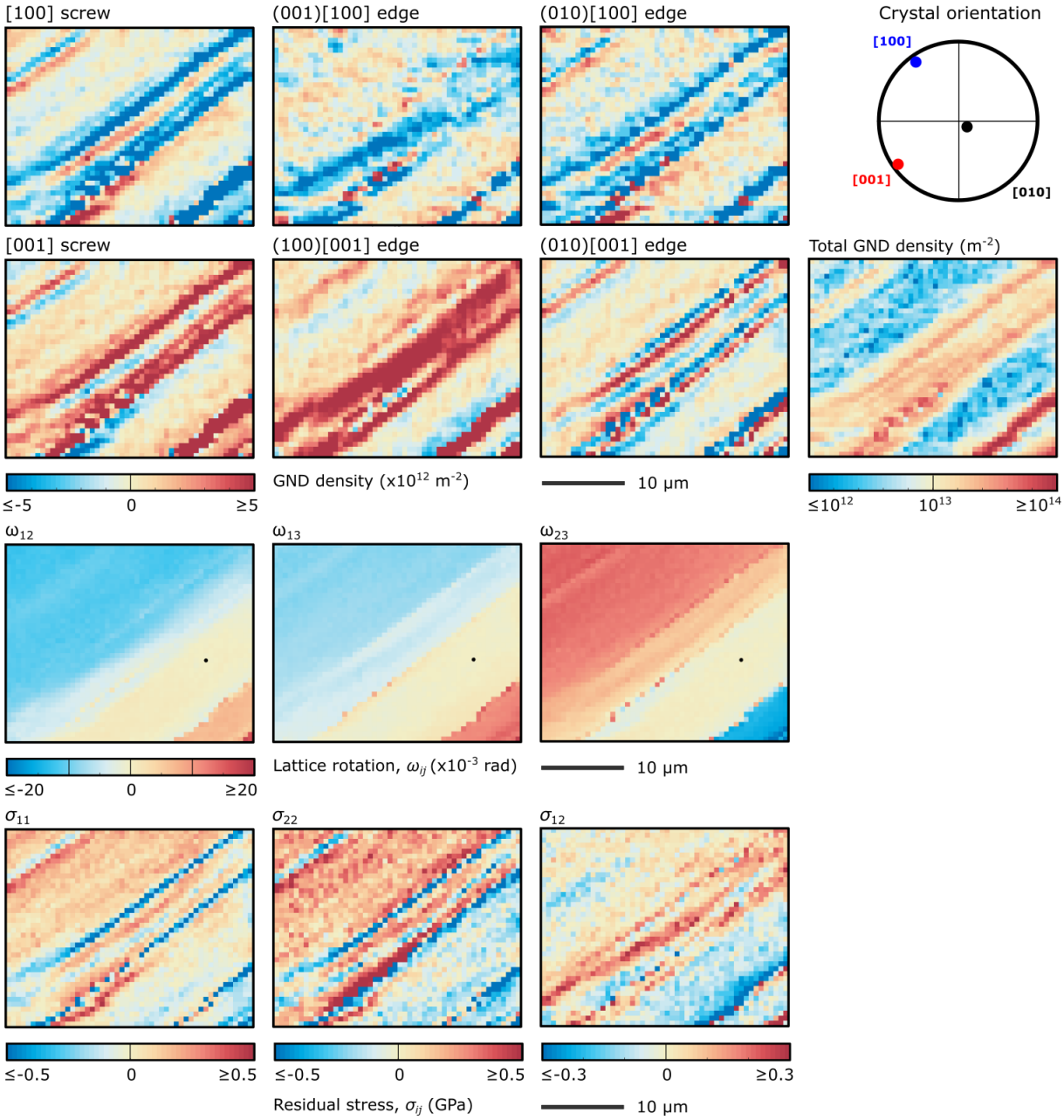

Figure 7: *LH17_HR6. HR-EBSD results of a different grain in sample LH17 compared to Figures 5 and 6. The six maps at the top present the GND densities of the different dislocation types, where the colours indicate opposing signs of the burgers vector. The crystal orientation is presented in the top right and below it the total GND density is presented. The third row of maps presents the lattice rotation, ω_{ij}. The black dot indicates the reference point for the calculations of the lattice rotations. The bottom row presents the maps of the residual stresses, σ_{ij}, where σ_{12} represents the residual shear stress. The step size is 0.6 μm and the number of datapoints is 2000 (50×40).*

The HR-EBSD data provides the shear stresses required in equation (2) to calculate the restricted second moment, $v_2(\sigma_{12})$ (Groma & Bakó, 1998; Wilkinson et al., 2014). Figure 8 demonstrates that the restricted second moment for each HR-EBSD map plots as a straight line when plotted against $\ln(\sigma_{12})$. Similar to the experimental results in Wallis et al. (in prep.), the presence of these straight lines means that $P(\sigma_{12}) \propto \sigma_{12}^{-3}$ and that therefore the stress fields are assumed to be generated by dislocations (Wilkinson et al., 2014; Wallis et al., in prep.).

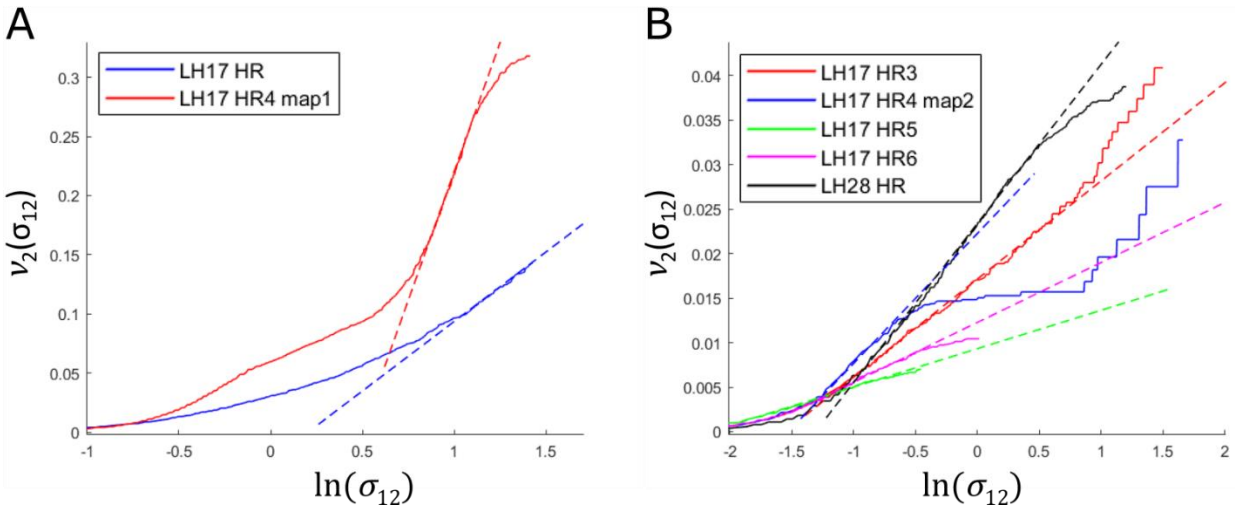

Figure 8: *Restricted second moments of the shear stresses plotted against the natural log of the shear stresses. Shear stresses are obtained by HR-EBSD of which all obtained maps by this research are plotted. The dashed lines indicate that all results presented here have a straight part at high stresses, meaning that* $P(\sigma_{12}) \propto \sigma_{12}^{-3}$. *Maps LH17_HR, LH17_HR4_map2 and LH17_HR6 correspond to Figures 5, 6 and 7, respectively. The other HR-EBSD maps can be found in the supplementary data.*

4. Discussion

The MIPFs and the HR-EBSD results combined suggest a dominant dislocation type that forms the subgrain boundaries. The HR-EBSD results (Figures 5, 6 and 7) demonstrate that subgrain boundaries are dominantly oriented perpendicular to the [100] axis and that dislocation types with a [100] burgers vector are more abundant than those with a [001] burgers vector in the GND maps (in Figures 5 and 6). The MIPFs (Figure 3) reveal elevated densities between [010] and [001], suggesting dominant slip systems with [100] burgers vectors forming subgrain boundaries. The main peaks in the MIPFs correspond to [010] misorientation axes. These [010] misorientation axes combined with the observation that the subgrain boundaries are perpendicular to the [100] axis in the HR-EBSD maps result in a dominant (001)[100] dislocation type in the formation of subgrain boundaries.

Screw dislocations play a role in the formation of subgrain boundaries as well. The MPFs (Figure 4) suggest a combination of twist walls and tilt walls, meaning that both edge and screw dislocations are important in subgrain boundary formation. HR-EBSD reveals high GND densities for both types of screw dislocations in the samples, localized in the high-density bands. Wallis et al. (2017) reveals strong correlations between the two screw dislocation types and the (001)[100] edge dislocations in an experiment on a deformed olivine single crystal at a temperature of 1000°C, where low-temperature plasticity likely occurred. This correlation means that the dislocations interact with each other via glide forces (as described by the Peach-Koehler equation in Peach & Koehler, 1950). In their research, Wallis et al. (2017) discuss that these correlations result from mixed boundaries of twist and tilt walls, corresponding to the interpretations in the current research.

Wallis et al. (2017) also demonstrates that the stress fields of the (100)[001] and (001)[100] edge dislocations can interact via glide forces. Figure 7 of the current research reveals that that these two dislocation types together form a shared banded structure, which is likely caused by this interaction via glide forces. The orientation of the banded structures are observed to be, similar to the subgrain boundaries, perpendicular to the [100] direction. This orientation suggests that the (100)[001] edge dislocations form slip bands at the same locations where the (001)[100] edge dislocations pileup towards subgrain boundaries. Because of the stress interactions via glide forces, both dislocation types will contribute to the build up of stresses. As mentioned before, screw dislocations also interact with the edge dislocation types, contributing to the build up of stress as well. All of these interactions will make glide more difficult where the dislocations pile up, resulting in strain hardening.

Other similarities between the current research and the sample deformed at 1000°C of Wallis et al. (2017) are found in the banded structure of the samples and the stress heterogeneity. Similar to the current research, Wallis et al. (2017) reveals equally spaced bands (on the scale of several micrometres) of elevated GND density with alternating burgers vectors. In the experimental results there are multiple sets of structures, but the current research contains only one clear set of banded structures. In this set the edge dislocations with a [100] burgers vector seem to contribute to subgrain boundaries at the same location where the edge slip systems with a [001] burgers vector form slip bands. However, the banded structure results in local stress heterogeneities of hundreds of MPa's on a length scale of a couple micrometres, similar to Wallis et al. (2017), Wallis et al. (2019b) and Wallis et al. (in prep.). Some of these experiments result in higher stress heterogeneities, but they also have much greater macroscopic differential stresses.

Figure 9 presents an interpretation of the GND density map of the (001)[100] edge dislocations, as presented in the results in Figure 6. This dislocation type is, as mentioned before, most likely the dominant slip system in subgrain boundary formation as a result from the HR-EBSD data and the MIPFs. The subgrain boundary is present in both figures 9A and 9B at number 4, organised as a column of aligned dislocations. This is the commonly accepted structure for edge dislocations forming a tilt boundary. On the right of the subgrain boundary the GND density is low, but on its left side there are two bands of high GND density with opposing burgers vectors (coloured red and blue in Figure 9A). These two bands are indicated by the numbers 1 and 3. The area in between them, indicated by number 2 in the figure, has a low GND density, but probably consists of dipole pairs of dislocations. These dipole pairs need dislocation climb to annihilate, which is minimal at the relatively low temperature of the sample. Dipole pairs do not contribute to the lattice curvature and therefore do not create a high GND density. Similar to the dislocation decorated samples in Figure 4, the dislocations pile up towards the subgrain boundary which acts as an obstacle. The stress fields of the individual dislocations interact with each other, creating back stresses. These back stresses are horizontal in this figure, since the burgers vector of the dislocations here are also horizontal. This compares well to the observed shear stresses (σ_{12}) in Figure 6, which reveal heterogeneity also perpendicular to the subgrain boundary. Furthermore, the (010)[100] edge dislocations in Figure 6 have a similar structure as the (001)[100] dislocations. Wallis et al. (2017) demonstrates that the stress fields of these two dislocation types are unable to interact with each other via glide forces. However, both of these dislocation types interact with the [100] screw dislocations, raising the question how much the (010)[100] edge dislocations contribute to the strain hardening.

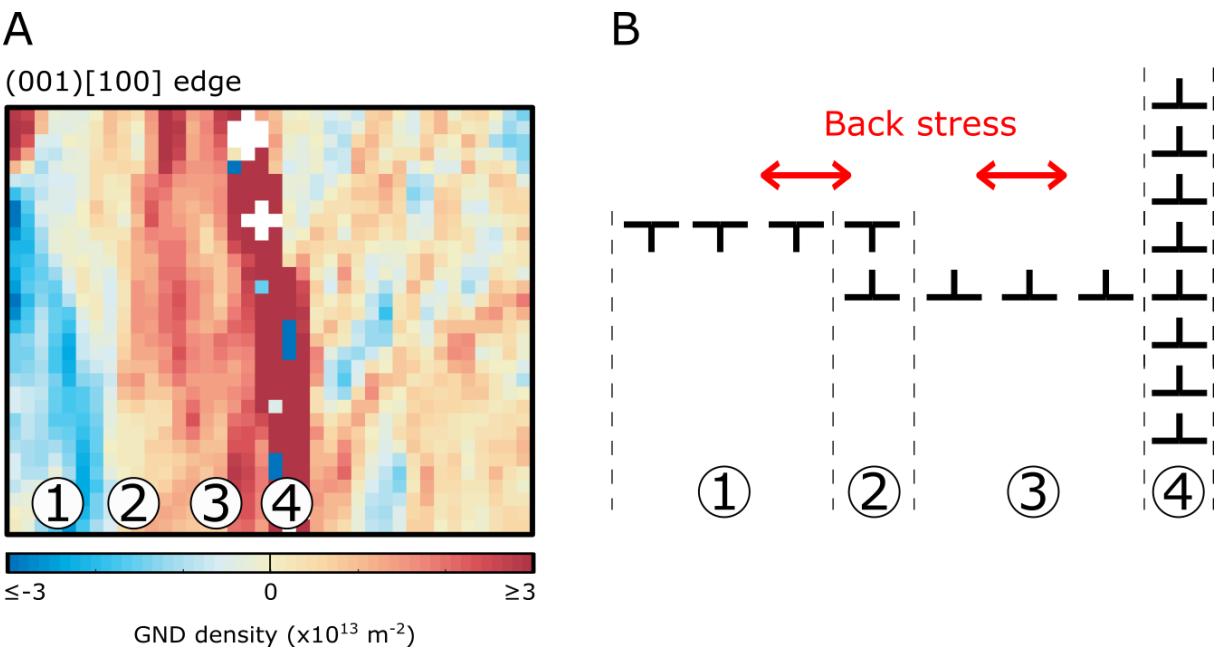

Figure 9: *Interpretation of the GND density of the (001)[100] edge dislocation type. A) The same GND density map as in Figure 6. The numbers in the map correspond to the numbers in the interpretation on the right. B) The simplified interpretation of the structure of the dislocations. Number 1 in this figure illustrates the structure of the band of dislocations with a negative sign, number 2 the dipole pairs of dislocations, number 3 the band of dislocations with a positive sign and number 4 the subgrain boundary. The burgers vectors are horizontal in this figure, causing the dislocations to pile up, creating back stresses in the same orientation.*

The dominant slip system found in this research, (001)[100] edge, correlates with an E-type CPO. The conditions of this type of CPO match the expectations of the geological setting, where it often corresponds to a wet environment and relatively low stress (Bernard et al., 2019). The conventional EBSD analysis on CPO types (Figure 3) does however result in a dominant B-type CPO. This can be the result of a different deformation phase, since it would be expected for rocks in this setting to have seen multiple deformation phases. The presence of at least one other deformation phase can also explain the different set of more chaotic oriented dislocations observed in the decorated samples (Figures 4A and 4C).

The distance from the metamorphic sole does not seem to change the microstructure significantly, based on the results of this research. As the distance from the sole increases, the petrology of the peridotites changes (Ambrose et al., 2018) as well as the influence of the sole itself in terms of temperature. The conventional EBSD results (Figure 3) reveal that the dominant CPO type and misorientation axes are clearest close to the sole, but do not clearly shift to other outcomes further from the sole. The results of the oxidation decoration also demonstrate that the structures are similar in the samples, regardless of their distance from the sole. Therefore this research assumes that the HR-EBSD data at 51 m from the sole is representative for the other samples as well.

Overall, the results of the current research on natural peridotites corresponds well to the experimental research on olivine (e.g., Wallis et al., 2017, 2019b, in prep.; Hansen et al., 2019). The microstructures in the samples contain a significant heterogeneity in dislocation density and residual shear stress on a scale of a few micrometres, of which the latter reaches differences of several hundreds of megapascals. Analysis of the residual shear stresses indicates a relation between the probability and the high stresses (Figure 8), meaning that $P(\sigma_{12}) \propto \sigma_{12}^{-3}$. This relation indicates that the stress heterogeneity is most likely caused by long-range interactions between dislocations (Wallis et al., in prep.), illustrated as the back-stresses in the conceptual model in Figure 9. This means that the natural peridotites used in this research support the applicability of the new flow law for transient creep in olivine (Figure 1), based on the back stresses between dislocations (Hansen et al., 2019).

These results might not only be applicable to the low-temperature locations within the subduction zone, but also to the locations where the temperatures are higher. Previous research on experimentally deformed olivine demonstrates that samples deformed at 25°C and samples deformed at 1150−1250°C exhibit very similar stress heterogeneities (Wallis et al., 2019b, in prep.). The current research, with naturally deformed peridotites at 770−990°C, contributes to these experiments by demonstrating the relevance for natural settings. These results combined suggest that the flow law is applicable at higher temperatures as well, where the microstructures might however be less preserved. With this temperature range and the demonstrated relevance to natural rocks, the new flow law by Hansen et al. (2019) improves large-scale modelling of plate-boundary fault zones by including short-term, time-dependent stress and strength changes.

5. Conclusions

This research demonstrates that olivine deformed at low temperature in natural peridotites contains similar microstructures compared to experiments on low-temperature plasticity in olivine. The dislocations in the natural samples form a banded structure of high dislocation density parallel to the [001] direction, where the (001)[100] edge dislocations and both types of screw dislocations are found to be dominant in subgrain boundary formation. Both the experiments and the natural samples contain stress heterogeneities of hundreds of MPa's on a length scale of only a few micrometre. Analysis of the residual shear stress reveals that the stress heterogeneity originates from long-range interactions between dislocations (i.e., back stresses). This supports the applicability of the new flow law for low-temperature plasticity in olivine.

Acknowledgements

I thank my first supervisor, David Wallis, for providing samples for this study and for discussions, feedback and guidance during the entire project. I thank Maartje Hamers and André Niemeijer for their assistance in performing oxidation decoration and Oliver Plümper for being my second supervisor. I also thank my fellow students Ilse Pluim, Jort Jansen, Olivier Winkel, Dieuwertje Kuypers, Boris Gesbert and Maurits Beudeker for their feedback and support during my project.

References

Agard, P., Yamato, P., Soret, M., Prigent, C., Guillot, S., Plunder, A., et al. (2016). Plate interface rheological switches during subduction infancy: Control on slab penetration and metamorphic sole formation. *Earth and Planetary Science Letters, 451*, 208−220.

Ambrose, T. K., Wallis, D., Hansen, L. N., Waters, D. J. & Searle, M. P. (2018). Controls on the rheological properties of peridotite at a palaeosubduction interface: A transect across the base of the Oman-UAE ophiolite. *Earth and Planetary Science Letters, 491*, 193−206.

Ashby, M. F. & Duval, P. (1985). The creep of polycrystalline ice. *Cold Regions Science and Technology, 11,* 285−300.

Bernard, R. E., Behr, W. M., Becker, T. W. & Young, D. J. (2019). Relationships between olivine CPO and deformation parameters in naturally deformed rocks and implications for mantle seismic anisotropy. *Geochemistry, Geophysics, Geosystems, 20,* 3469−3494.

Britton, T. B., & Wilkinson, A. J. (2011). Measurement of residual elastic strain and lattice rotations with high resolution electron backscatter diffraction. *Ultramicroscopy, 111(8),* 1395−1404.

Britton, T. B., & Wilkinson, A. J. (2012). High resolution backscatter diffraction measurements of elastic strain variations in the presence of larger lattice rotations. *Ultramicroscopy, 114,* 82−95.

Cooper, R. F., Stone, D. S. & Plookphol, T. (2016). Load relaxation of olivine single crystals. *Journal of Geophysical Research: Solid Earth, 121,* 7193−7210.

De Kloe, R., Drury, M. & Farrer, J. K. (2002). Determination of activated slip systems in experimentally deformed olivine-orthopyroxene polycrystals using EBSD. *Microscale Microanalyses, 8 (2),* 680−681.

Durham, W. B., Froidevaux, C. & Jaoul, O. (1979). Transient and steady-state creep of pure forsterite at low stress. *Physics of the Earth and Planetary Interiors, 19,* 263−274.

Duval, P., Ashby, M. F. & Anderman, I. (1983). Rate-controlling processes in the creep of polycrystalline ice. *The Journal of Physical Chemistry, 87,* 4066−4074.

Field, E. H., Biasi, G. P., Bird, P., Dawson, T. E., Felzer, K. R., Jackson, D. D., et al. (2015). Long-term time-dependent probabilities for the third Uniform California Earthquake Rupture Forecast (UCERF3). *Bulletin of the Seismological Society of America, 105(2A),* 511–543.

Freed, A. M. (2005). Earthquake Triggering by Static, Dynamic, and Postseismic Stress Transfer. *Annual Review of Earth and Planetary Sciences, 33(1),* 335–367.

Groma, I. & Bakó, B. (1998). Probability distribution of internal stresses in parallel straight dislocation systems. *Physical Review B, 58,* 2969−2974.

Han, S., Sauber, J. & Pollitz, F. (2014). Broadscale postseismic gravity change following the 2011 Tohoku-Oki earthquake and implication for deformation by viscoelastic relaxation and afterslip. *Geophysical Research Letters, 41(16),* 5797−5805.

Hansen, L. N., Kumamoto, K. M., Thom, C. A., Wallis, D., Durham, W. B., Goldsby, D. L., et al. (2019). Low-temperature plasticity in olivine: Grain size, strain hardening, and the strength of the lithosphere. *Journal of Geophysical Research: Solid Earth, 124,* 5427−5449.

Hansen, L.N., Wallis, D., and Kempton, I. (in prep.) A microphysical model for transient deformation of olivine from stress-reduction tests.

Hanson, D. R. & Spetzler, H. A. (1994). Transient creep in natural and synthetic, iron-bearing olivine single crystals: Mechanical results and dislocation structures. *Tectonophysics, 235,* 293−315.

Huang, R. & Li, W. (2014). Post-earthquake landsliding and long-term impacts in the Wenchuan earthquake area, China. *Engineering Geology, 182(B),* 111−120.

Jiang, J., Britton, T. B., & Wilkinson, A. J. (2013). Mapping type III intragranular residual stress distributions in deformed copper polycrystals. *Acta Materialia, 61(15),* 5895−5904.

Karato, S.-I. (1987). Scanning electron microscope observation of dislocations in olivine. Physics and *Chemistry of Minerals, 14(3),* 245−248.

Karato, S.-I. (1998). Micro-Physics of Post Glacial Rebound. *Dynamics of the Ice Age Earth: A Modern Perspective (ed. Wu, P.), 3−4,* 351−364.

Karato, S.-I. & Jung, H. (2003). Effects of pressure on high-temperature dislocation creep in olivine. *Philosophical Magazine, 83(3)*, 401−414.

Kohlstedt, D. L., Goetze, C., Durham, W. B. & Vander Sande, J. B. (1976). New technique for decorating dislocations in olivine. *Science, 191,* 1045−1046.

Mikami, Y., Oda, K., Kamaya, M. & Mochizuki, M. (2015). Effect of reference point selection on microscopic stress measurement using EBSD. *Materials Science and Engineering A, 647,* 256−264.

Peach, M., & Koehler, J. S. (1950). The forces exerted on dislocations and the stress fields produced by them. *Physical Review, 80,* 436-439.

Pollitz, F., Vergnolle, M. & Calais, E. (2003). Fault interaction and stress triggering of twentieth century earthquakes in Mongolia. *Journal of Geophysical Research: Solid Earth, 108(B10),* 2503.

Qiu, Q., Moore, J. D. P., Barbot, S., Feng, L., Hill, E. M. (2018). Transient rheology of the Sumatran mantle wedge revealed by a decade of great earthquakes. *Nature communications, 9,* 995.

Sun, T., Wang, K., Iinuma, T., Hino, R., He, J., Fujimoto, et al. (2014). Prevalence of viscoelastic relaxation after the 2011 Tohoku-Oki earthquake. *Nature, 514*, 84−87.

Wallis, D., Hansen, L. N., Britton, T. B. & Wilkinson, A. J. (2017) Dislocation Interactions in Olivine Revealed by HR-EBSD. *Journal of Geophysical Research, 122,* 7659−7678.

Wallis, D., Hansen, L. N., Britton, T. B. & Wilkinson, A. J. (2019a). High-angular resolution electron backscatter diffraction as a new tool for mapping lattice distortion in geological minerals. *Journal of Geophysical Research, 124(7),* 6337−6358.

Wallis, D., Hansen, L. N., Kumamoto, K. M., Thom, C. A., Plümper, O., Ohl, M., et al. (2019b) Dislocation interaction during low-temperature plasticity of olivine strengthen the lithospheric mantle. *EarthArXiv.* https://doi.org/10.31223/osf.io/hmp3k

Wallis, D., Hansen, L. N., Wilkinson, A. & Lebensohn, R. A. (in prep.). Stress fields of dislocations in olivine imply an intragranular contribution to transient creep of the upper mantle.

Wilkinson, A. J., Meaden, G., & Dingley, D. J. (2006). High-resolution elastic strain measurement from electron backscatter diffraction patterns: New levels of sensitivity. *Ultramicroscopy, 106(4−5),* 307−313.

Wilkinson, A. J., Tarleton, E., Vilalta-Clemente, A., Jiang, J., Britton, T. B. & Collins, D. M. (2014). Measurement of probability distributions for internal stresses in dislocated crystals. *Applied Physics Letters, 105,* 181907.

Appendix: Supplementary material

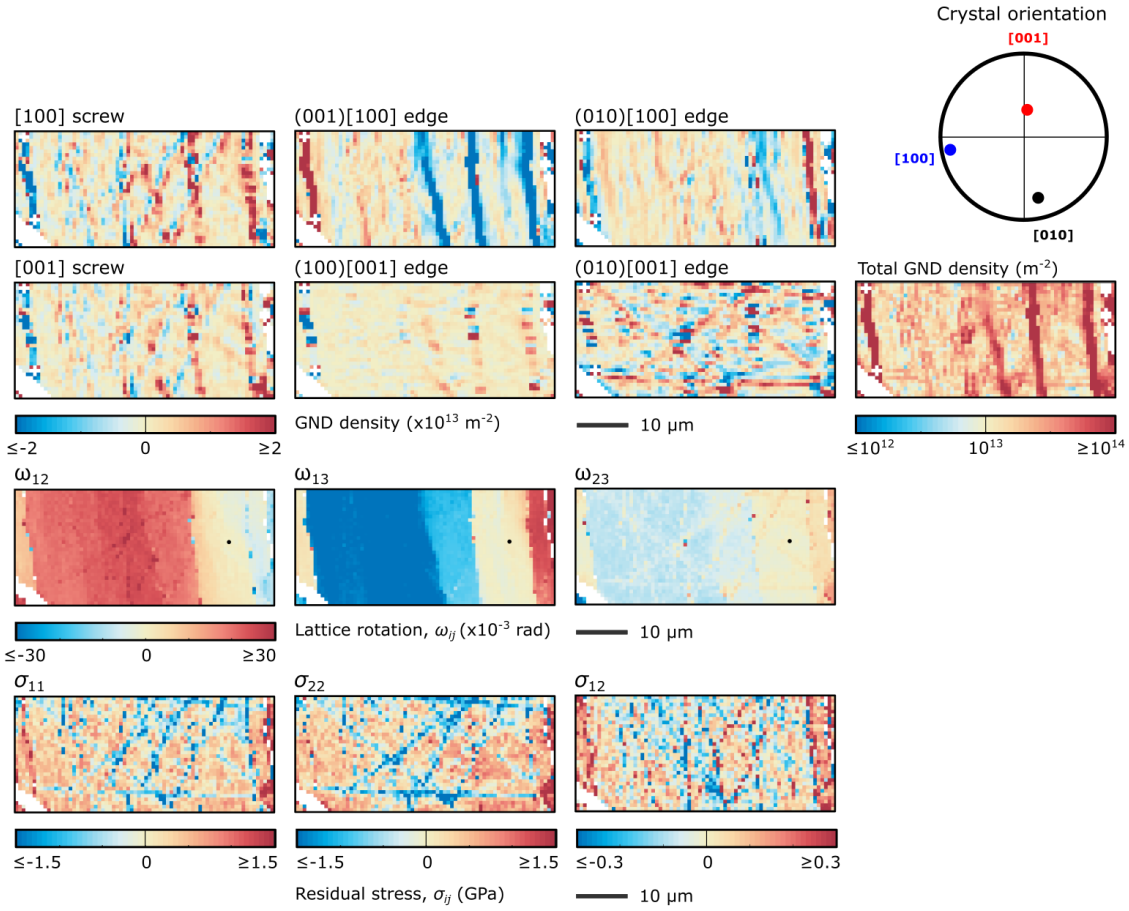

Figure S1: *LH17_HR3. HR-EBSD results of a part of the grain in figure 5 (sample LH17, located 51 m from the metamorphic sole). The six maps on the top show the GND densities of the different slip systems, where the colours indicate a positive or negative direction of the burgers vector. The crystal orientation is shown in the top right and below it the total GND density is shown. The third row of maps show the lattice rotation, ω_{ij}, in which grain boundaries (i.e., local misorientations greater than 10 degrees) are shown. The black dot shows the reference point for the calculations of the lattice rotations. The bottom row shows the residual stress, σ_{ij}, where σ_{12} represents the residual shear stress. The step size is 0.7 μm and the number of datapoints is 2304 (72×32).*

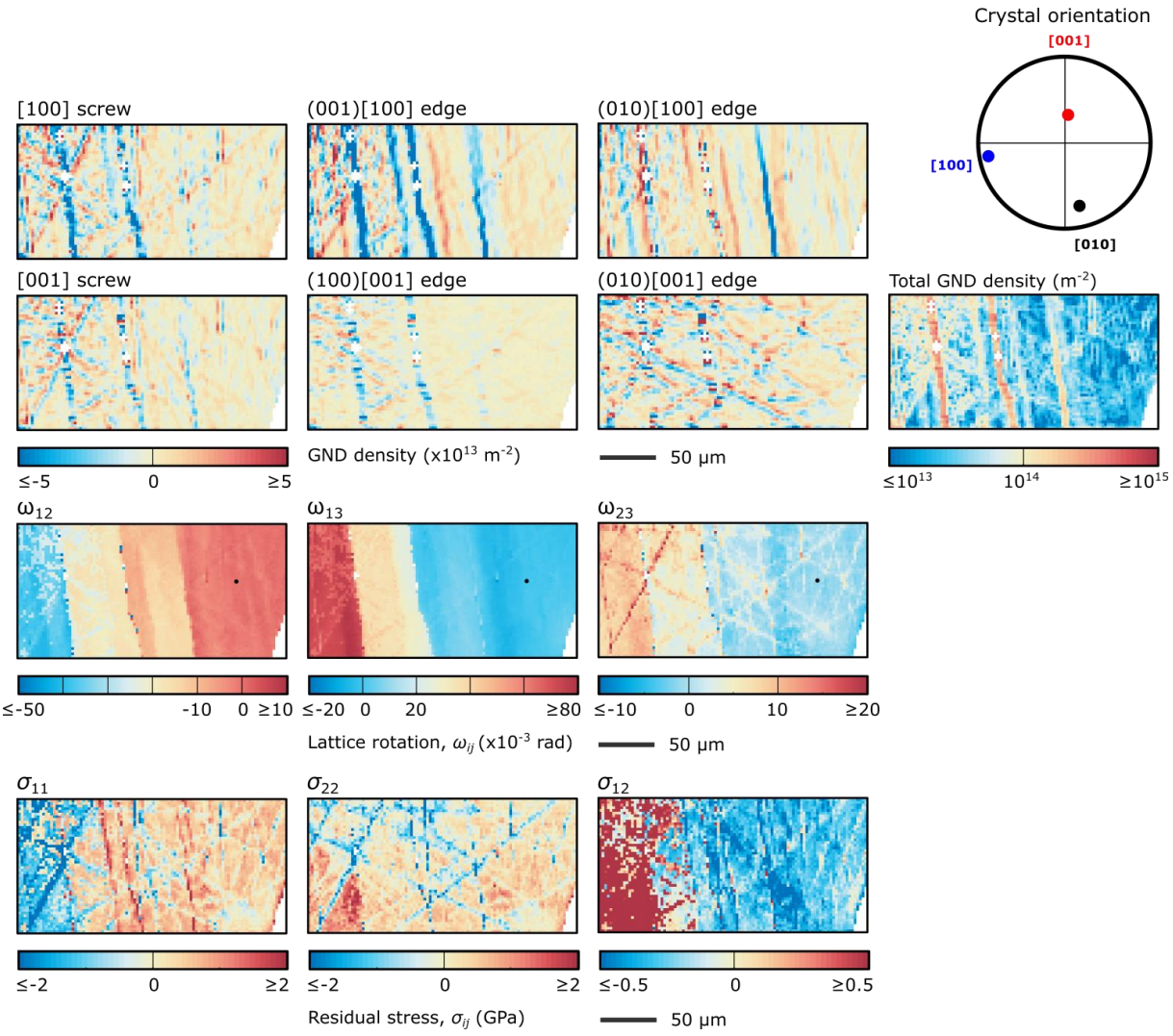

Figure S2: *LH17_HR4_map1. HR-EBSD results of a part of the grain in figure 5 (sample LH17, located 51 m from the metamorphic sole). The six maps on the top show the GND densities of the different slip systems, where the colours indicate a positive or negative direction of the burgers vector. The crystal orientation is shown in the top right and below it the total GND density is shown. The third row of maps show the lattice rotation, ω_{ij}, in which grain boundaries (i.e., local misorientations greater than 10 degrees) are shown. The black dot shows the reference point for the calculations of the lattice rotations. The bottom row shows the residual stress, σ_{ij}, where σ_{12} represents the residual shear stress. The step size is 0.4 µm and the number of datapoints is 5000 (100×50).*

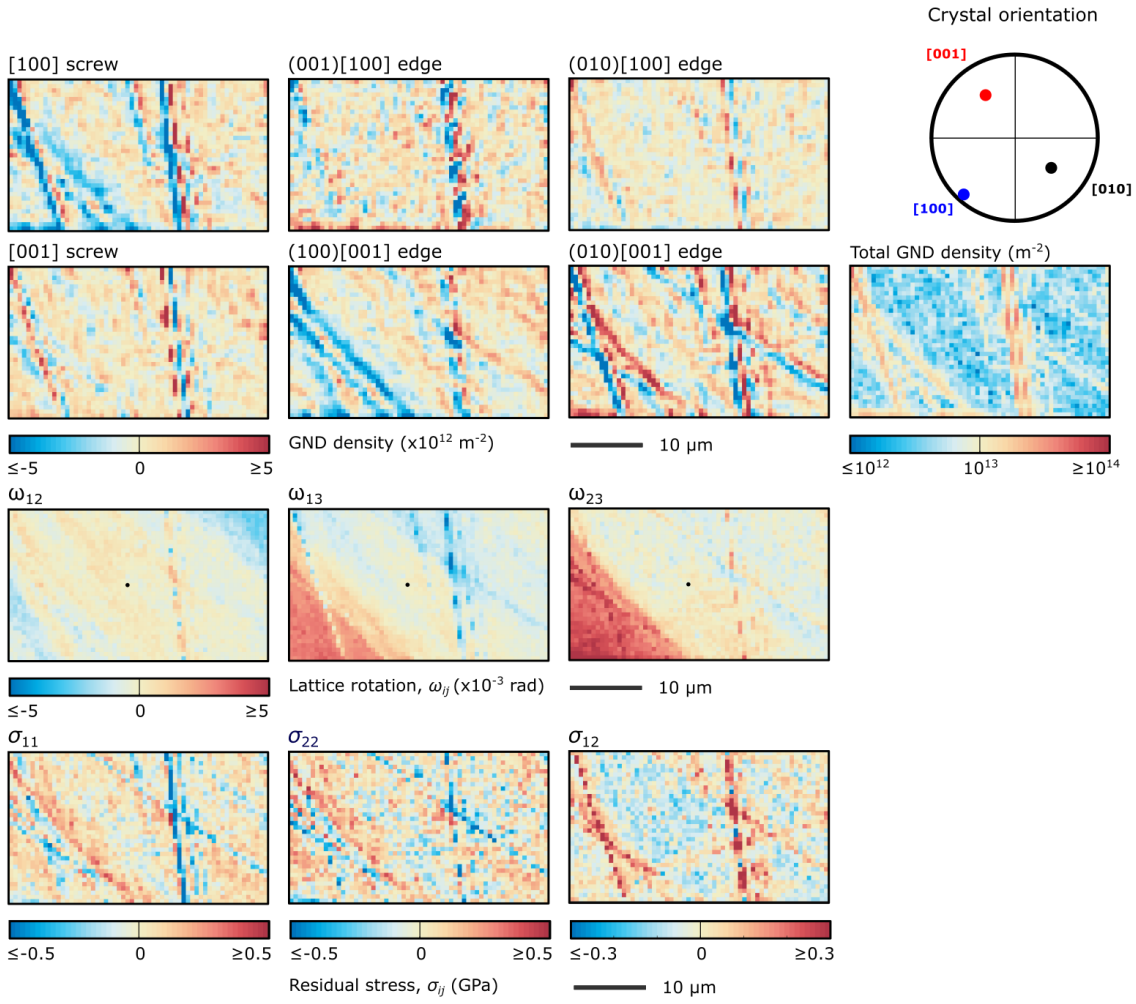

Figure S3: *LH17_HR5. HR-EBSD results of a different grain than figures 5, 6, 7, S1 and S2, but in the same sample (sample LH17, located 51 m from the metamorphic sole. The six maps on the top show the GND densities of the different slip systems, where the colours indicate a positive or negative direction of the burgers vector. The crystal orientation is shown in the top right and below it the total GND density is shown. The third row of maps show the lattice rotation, ω_{ij}, in which grain boundaries (i.e., local misorientations greater than 10 degrees) are shown. The black dot shows the reference point for the calculations of the lattice rotations. The bottom row shows the residual stress, σ_{ij}, where σ_{12} represents the residual shear stress. The step size is 0.6 µm and the number of datapoints is 2100 (60×35).*

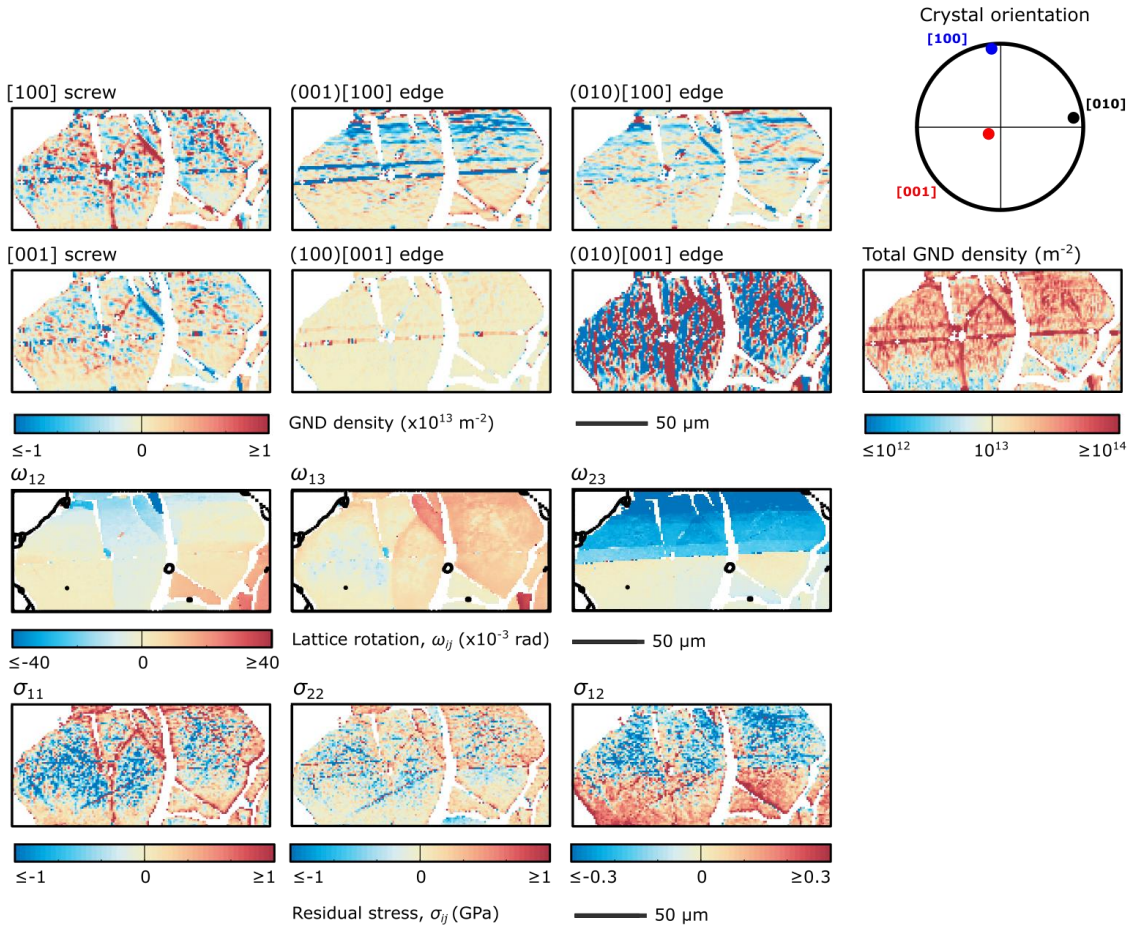

Figure S3: *LH28_HR. HR-EBSD results of a grain in sample LH28, 469 m from the metamorphic sole. The six maps on the top show the GND densities of the different slip systems, where the colours indicate a positive or negative direction of the burgers vector. The crystal orientation is shown in the top right and below it the total GND density is shown. The third row of maps show the lattice rotation, ω_{ij}, in which grain boundaries (i.e., local misorientations greater than 10 degrees) are shown. The black dot shows the reference point for the calculations of the lattice rotations. The bottom row shows the residual stress, σ_{ij}, where σ_{12} represents the residual shear stress. The step size is 1.2 µm and the number of datapoints is 10500 (150×70).*

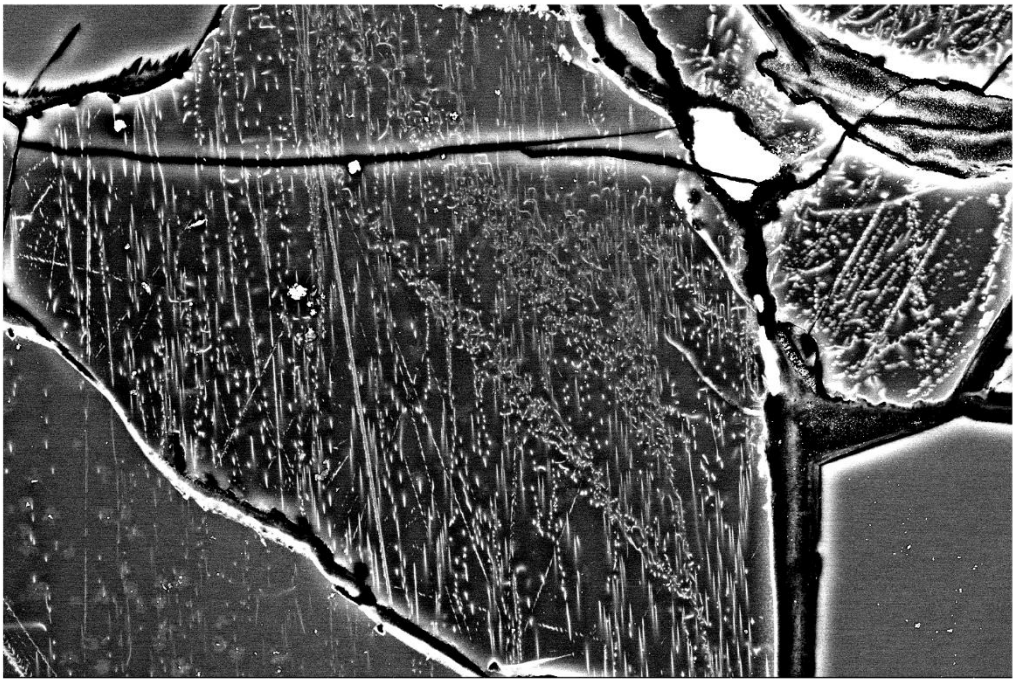

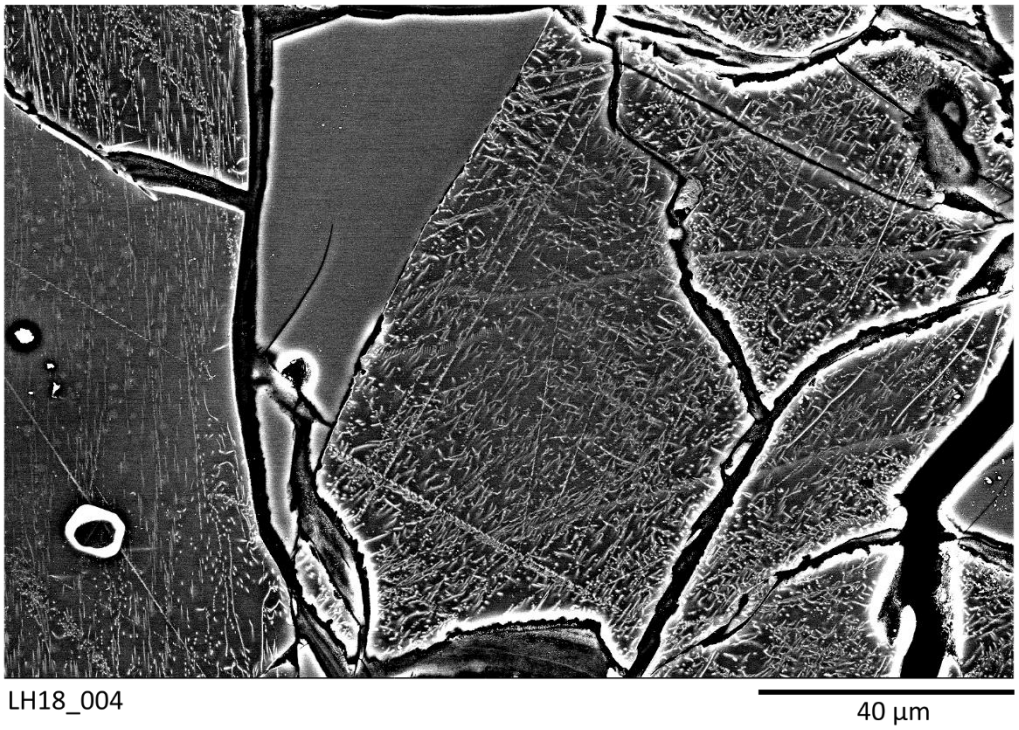

Figure S4: *Oxidation decoration results of sample LH18, 22 m from the sole. Figure 4A is zoomed in on the central part of LH18_001 here and Figure 4B is zoomed in on the central part of LH18_004 here.*

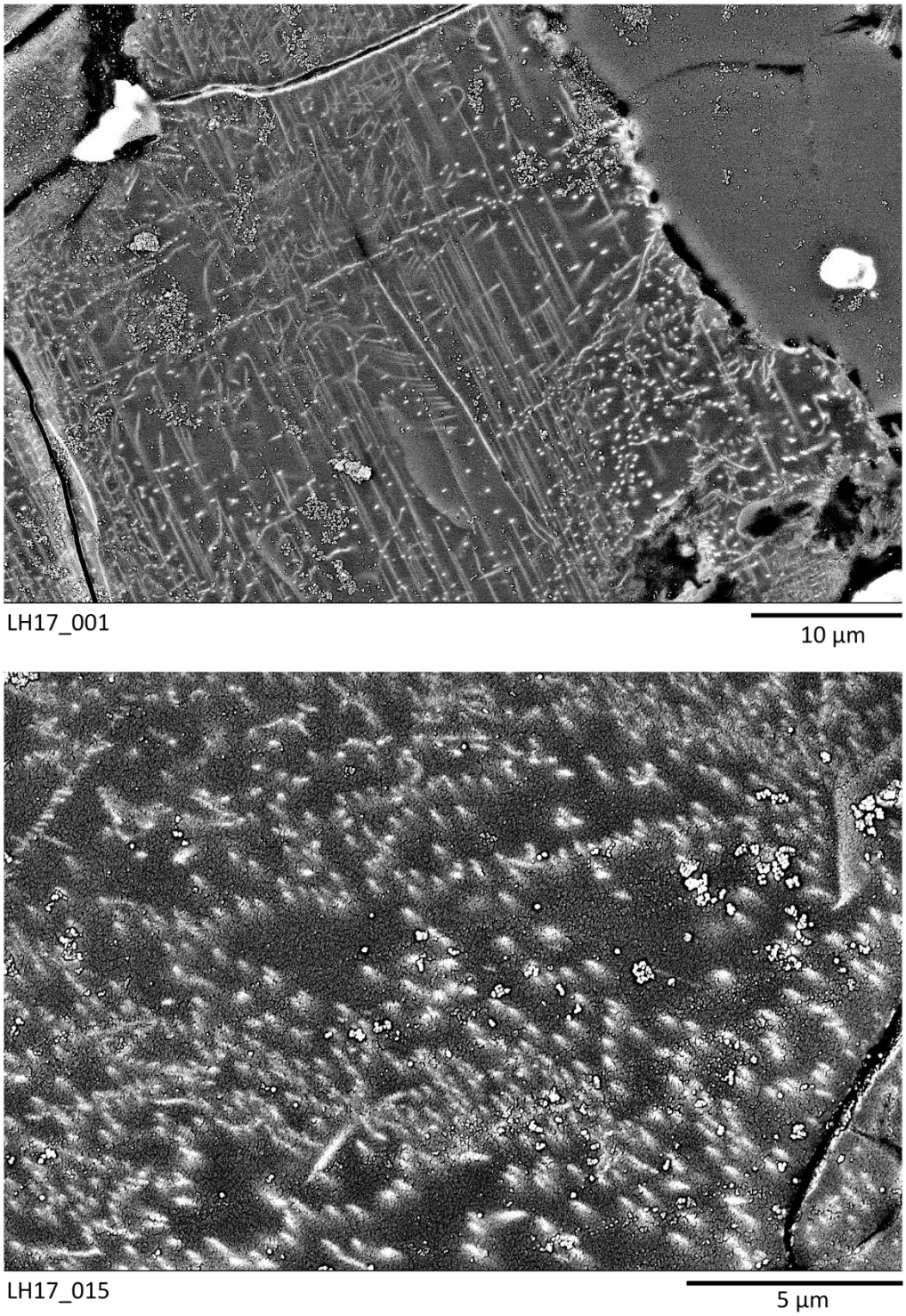

Figure S5: *Oxidation decoration results of sample LH17, 51 m from the sole. Both of the figures here contain a lot of surface imperfections, which show as bright white dots with (in contrast to the more dull white dots and lines which are dislocations).*

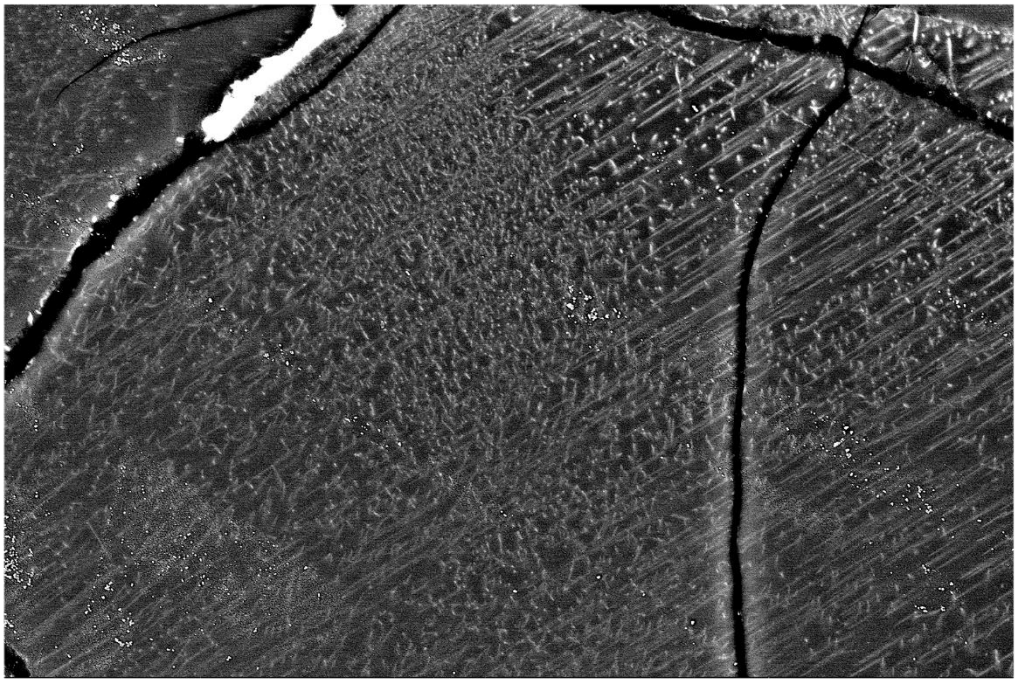

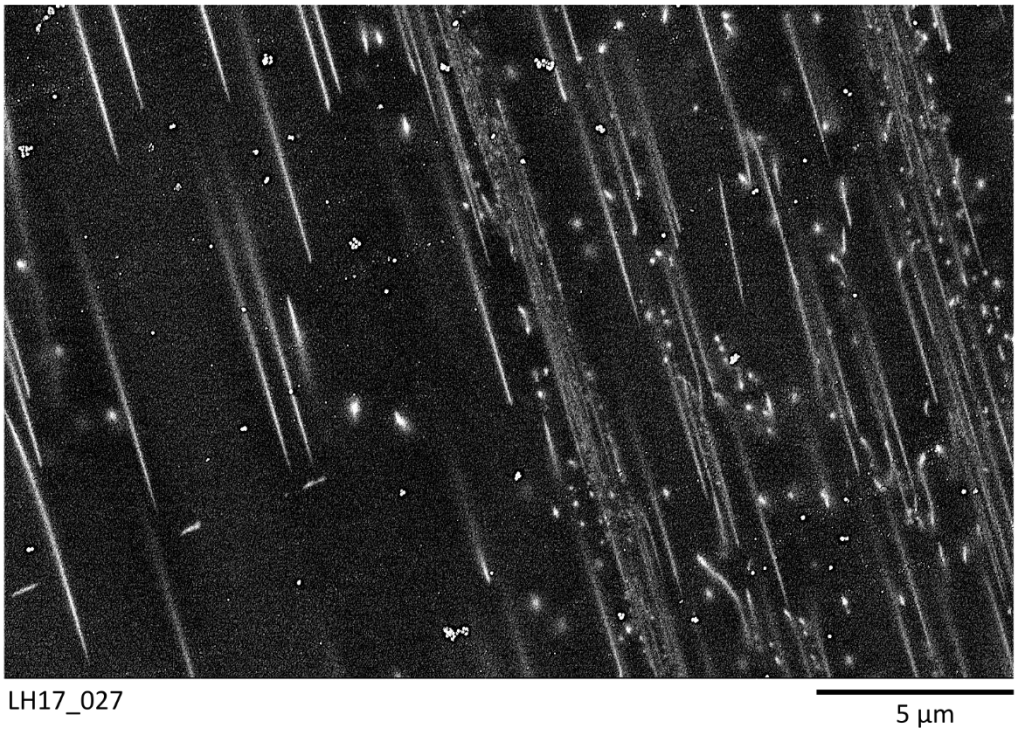

Figure S6: *Oxidation decoration results of sample LH17, 51 m from the sole. Figure 4C is zoomed in on the top right of LH17_023 and Figure 4D is the same as LH17_027.*

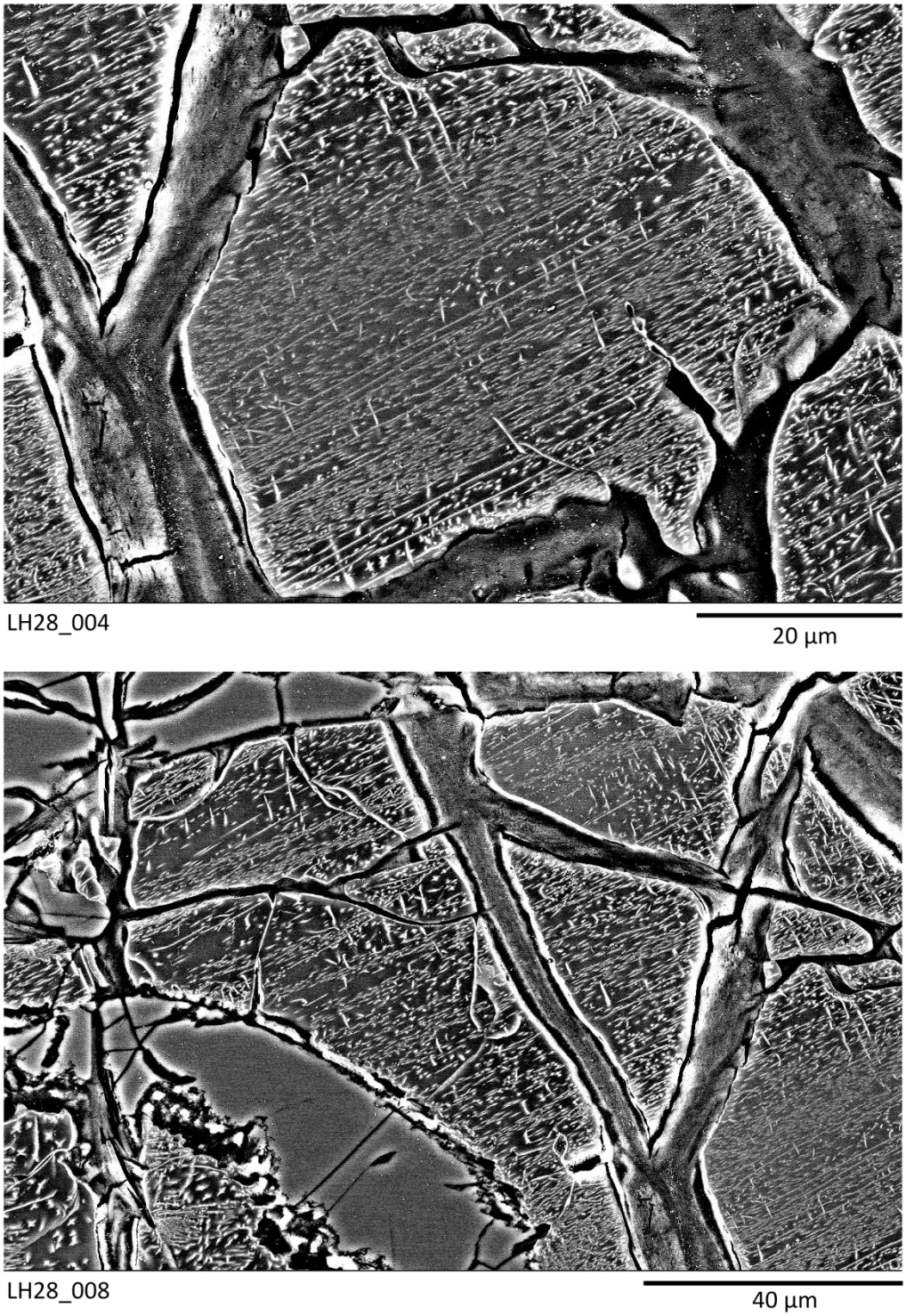

Figure S7: *Oxidation decoration results of sample LH28, located 469 m from the sole. Figure 4E zooms in just left of the centre of LH28_008.*

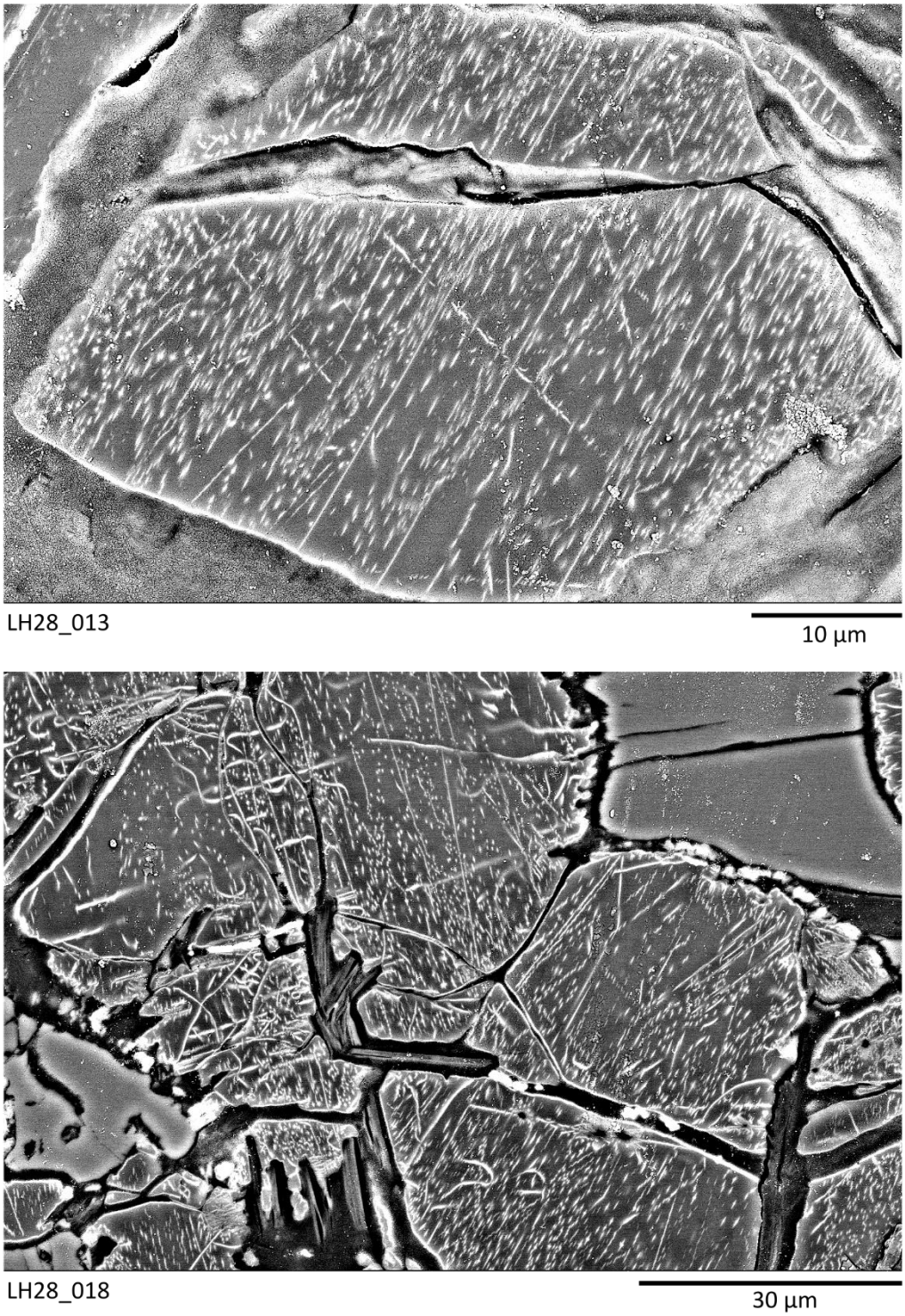

Figure S8: *Oxidation decoration results of sample LH28, located 469 m from the sole. Figure 4F zooms in on the central top part of LH28_018.*